
Research Article: Confirmation | Novel Tools and Methods

Quantitative evaluation in estimating sources underlying brain oscillations using current source density methods and beamformer approaches

<https://doi.org/10.1523/ENEURO.0170-19.2019>

Cite as: eNeuro 2019; 10.1523/ENEURO.0170-19.2019

Received: 8 May 2019

Revised: 24 June 2019

Accepted: 25 June 2019

This Early Release article has been peer-reviewed and accepted, but has not been through the composition and copyediting processes. The final version may differ slightly in style or formatting and will contain links to any extended data.

Alerts: Sign up at www.eneuro.org/alerts to receive customized email alerts when the fully formatted version of this article is published.

Copyright © 2019 Halder et al.

This is an open-access article distributed under the terms of the Creative Commons Attribution 4.0 International license, which permits unrestricted use, distribution and reproduction in any medium provided that the original work is properly attributed.

1

2 **1. Title: Quantitative evaluation in estimating sources underlying brain oscillations**3 **using current source density methods and beamformer approaches**4 **2. Abbreviated Title: Ground truth evaluation of inverse methods**5 **3. Authors:**

6 Tamesh Halder*, Siddharth Talwar*, Amit Kumar Jaiswal, Arpan Banerjee

7 *Both authors contributed equally (co-first authors)

8 **Affiliations**9 Cognitive Brain Dynamics Lab, National Brain Research Centre, NH-8, Manesar, Gurgaon - 122052,
10 Haryana, India11 **4. Author Contributions:** TH, ST and AB designed research; AKJ & AB collected data; TH, ST and AB
12 analyzed data; TH, ST and AB wrote the paper
1314 **5. Correspondence should be addressed to (include email address): arpan.nbrc@gov.in,**
15 **banerjee2007@gmail.com**16 **6. Number of Figures 7**17 **7. Number of Tables 1**18 **8. Number of
Multimedia NA**19 **9. Number of words for Abstract 284**20 **10. Number of words for Significance
Statement 95**21 **11. Number of words for Introduction 727**22 **12. Number of words for Discussion 941**23 **13. Acknowledgements**24 This work was supported by grants from the Department of Biotechnology, Govt. of India (Grant Nos
BT/RLF/Re-entry/31/2011 and BT/07/IYBA/2013) to A.B.25 **14. Conflict of Interest**

26 Authors report no conflict of interest

27 **15. Funding sources**28 Department of Biotechnology, Govt. of India (Grant Nos BT/RLF/Re-entry/31/2011 and
29 BT/07/IYBA/2013) to AB

30

1 Quantitative evaluation in estimating sources 2 underlying brain oscillations using current source 3 density methods and beamformer approaches

4 Abstract

5 Brain oscillations from electro-encephalogram (EEG) and magneto-encephalogram (MEG) shed light
6 on neurophysiological mechanisms of human behavior. However, to extract information on cortical pro-
7 cessing, researchers have to rely on source localization methods that can be very broadly classified into
8 current density estimates such as exact low resolution electromagnetic tomography (eLORETA), min-
9 imum norm estimates (MNE) and beamformers such as Dynamic Imaging of Coherent Sources (DICS)
10 and Linearly Constrained Minimum Variance (LCMV). These algorithms produce a distributed map
11 of brain activity underlying sustained and transient responses during neuroimaging studies of behav-
12 ior. On the other hand, there are very few comparative analyses that evaluates the “ground truth
13 detection” capabilities of these methods. The current article evaluates the reliability in estimation of
14 sources of spectral event generators in the cortex using a two-pronged approach. First, simulated EEG
15 data with point dipoles and distributed dipoles are used to validate the accuracy and sensitivity of each
16 one of these methods of source localization. The abilities of the techniques were tested by comparing
17 the localization error, focal width, false positive ratios while detecting already known location of neural
18 activity generators under varying signal to noise ratios. Second, empirical EEG data during auditory
19 steady state responses (ASSR) in human participants were used to compare the distributed nature
20 of source localization. All methods were successful in recovery of point sources in favorable signal
21 to noise scenarios and could achieve high hit rates if false positives are ignored. Interestingly, focal
22 activation map is generated by LCMV and DICS when compared to eLORETA while control of false
23 positives is much superior in eLORETA. Subsequently drawbacks and strengths of each method are
24 highlighted with a detailed discussion on how to choose a technique based on empirical requirements.

25

26

27 **Significance statement**

28 State-of-the-art methods of source localization techniques, e.g., current density methods, minimum
29 norm estimates and beamformers report distributed brain activity patterns that are often not in
30 consensus for a putative task. This article offers ground truth validation of these techniques in the
31 context of different kind of source detections, e.g., determining the sources underlying key events
32 (evoked potentials) and steady state brain oscillations (band limited brain activity). The broader goal
33 is to help cognitive neuroscientists select the most effective source localization technique that is in
34 sync with the signal processing needs required for targeting a specific question.

35 **1 Introduction**

36 Cortical oscillations play an important role in governing basic cognitive functions (Edelman and Mountcastle,
37 1978; Bressler and Kelso, 2001; Buzsáki and Draguhn, 2004). Several researchers have suggested that
38 electromagnetic brain activity at specific frequency bands carries meaningful information about neu-
39 ral function, e.g. alpha waves at 10 Hz (Bollimunta *et al.*, 2008; Llinás *et al.*, 1999), beta at 15-
40 30 Hz (Brovelli *et al.*, 2004), gamma at 30 Hz and above (Bressler *et al.*, 1993; Varela *et al.*, 2001;
41 Cheyne and Ferrari, 2013). Concurrently, time-locked transient responses have been useful for decades
42 in electrophysiological research, both for understanding basic neurobiological functions as well as in
43 clinical and other applications (Picton *et al.*, 1974; Kutas *et al.*, 1977; Pantev *et al.*, 1995; Clark *et al.*,
44 1995; Cheyne *et al.*, 2006). Hence, identifying the neural generators of sustained cortical oscillations
45 and task-specific transient neural responses from electro-encephalography/ magneto-encephalography
46 (EEG/ MEG) is an extensive topic of research. Once identified with adequate reliability, the focal
47 localization of sources will eventually reveal the underlying large-scale network governing cognitive
48 tasks.

49 There are several source localization methods in the literature, commonly known under the um-
50 brella of inverse methods (Hämäläinen and Sarvas, 1989). Most of these techniques are based on fitting
51 single/ multiple dipolar cortical source/sources within a defined cortical volume based on some as-
52 sumptions about relationships between the sources (Hämäläinen and Ilmoniemi, 1994; Van Veen *et al.*,
53 1997; Ishii *et al.*, 1999; Gross *et al.*, 2001; Hillebrand and Barnes, 2003; Liu *et al.*, 2002; Sato *et al.*,

54 2004). Some methods consider sources to have minimum correlation, e.g. synthetic aperture mag-
55 netometry (SAM) (Hillebrand and Barnes, 2003), linearly constrained minimum variance spatial fil-
56 tering (LCMV) (Van Veen *et al.*, 1997; Murzin *et al.*, 2011). There are specialized measures that
57 detect generators of oscillatory brain signals by considering maximum coherence between prospective
58 sources, e.g., dynamic imaging of coherent sources (DICS) (Gross *et al.*, 2001) and entropy based
59 metrics (Lina *et al.*, 2014). DICS is a frequency domain extension of beamforming methods over
60 the initially developed time-domain beamformers, e.g., LCMV and synthetic aperture magnetometry
61 (SAM) (Ishii *et al.*, 1999) that are primarily used for determining the sources underlying time-locked
62 ERP/ERF components. In EEG, where deeper sources can affect scalp potentials, current density
63 techniques such as minimum norm estimates (MNE) (Hämäläinen and Ilmoniemi, 1994) and exact
64 low-resolution brain electromagnetic tomography (eLORETA) (Pascual-Marqui, 2007) has been the
65 method of choice. Though, dynamic statistical parametric mapping (dSPM) (Liu *et al.*, 2002) and
66 sparse Bayesian learning (SBL) (Ramírez *et al.*, 2010) has been developed to improve upon the esti-
67 mates of spatial filter detection, eLORETA is still by far one of the most robust methods for EEG
68 source localization. eLORETA directly estimates current source density, a biophysically relevant pa-
69 rameter over a grid of plausible cortical locations for both detection of time-locked activity e.g., in
70 event related potentials / fields (ERP/ERF) or frequency-locked activity e.g., spontaneous frequency
71 bursts or steady state oscillatory responses to a periodic stimuli. Nonetheless, the source estimated
72 by all methods are broadly influenced by depth, signal to noise strength of the neural activity, as
73 well as the the correlation in the covariance of the signals (Belardinelli *et al.*, 2012) and redundant
74 informational content of high temporal resolution data. Often these manifest in distributed source
75 activity estimation with diminished statistical power.

76 The accuracy of the location of neural activity along with lower false positives should be the
77 expectation from any source localization technique. In this article, we evaluate the performance of
78 the key current density techniques: eLORETA, MNE and beamformer approaches: DICS and LCMV
79 on simulated EEG data. Since LCMV and DICS belong to the same class of beamformers, they
80 were compared against eLORETA, to quantify localization efficiency between beamformers vs current
81 density measures. We compared the results from eLORETA and DICS on a paradigm of evoked
82 40-Hz auditory steady state responses (ASSR) and eLORETA, MNE and LCMV for detecting the
83 source of N100 activity when the same data was epoched time-locked to the stimulus onset. Many

84 inverse methods can localize a transient or steady state response or both. However, the biological
85 relevance or interpretation of these different information processing events can be very distinct. There
86 are comparison studies that evaluate the performance across different methods e.g., Bradley *et al.*
87 (2016); Hedrich *et al.* (2017) or sometimes the performance of detecting a focal cortical source across
88 modalities EEG and MEG, e.g., Srinivasan *et al.* (2006); Mideksa *et al.* (2015). In this article, our
89 focus was to compare the specificity and sensitivity of some of the prominent algorithms primarily
90 chosen based on their conceptual difference current density estimate vs beamforming to provide a basis
91 for choosing one above the other when faced with the issues of transient or steady state response. Very
92 rigorous comparison metrics e.g. localization error, spatial spread and false positive percentage were
93 used to evaluate accuracy and sensitivity of results along with an evaluation of the performance of these
94 methods at different depths of dipole placement in the simulated EEG data. Subsequently, empirical
95 EEG data during N100 and auditory steady state responses (ASSR) were used to draw comparisons
96 among distributed nature of source activity patterns generated by these methods.

97 2 Materials and Methods

98 2.1 Generation of synthetic EEG data:

99 To localize the oscillatory activity, as well as the transient response, we simulated a time-varying
100 sinusoid at 40 Hz and a mixture of Gaussian pulses, respectively. Both generated signals were free of
101 noise, and were consequently added to the acquired empirical baseline, for realistic noise simulation.
102 The magnitude of the dipolar source dynamics in cortical locations are represented by

$$q_i(t) = \sin(2\pi 40t) + \epsilon(0, \sigma) \quad (1)$$

103 where $q_i(t)$ is the electric dipole moment at location i and at time t , ϵ is white noise with zero mean
104 and standard deviation σ . We compared 3 conditions with respect to number of sources, by placing
105 single point dipole, two-points dipoles and distributed dipoles in a MNI brain template according
106 to the Montreal Neurological Institute (Müller and Weisz, 2012). Single point source was placed at
107 around the superior temporal region, in the left hemisphere (MNI coordinates: $(-60, -28, 6)$). Two
108 sources were placed, one in the left hemisphere (MNI coordinates: $(-60, -28, 6)$) and the other in

109 the right hemisphere (MNI coordinates: (64, -24, 6)) around the superior temporal region. Approxi-
 110 mately, hundred point sources were placed within a spherical volume with radius of 12 mm in the left
 111 hemisphere centred around superior temporal region at (-60, -28, 6), according to brain template.
 112 Another set of hundred point sources were placed around right hemisphere auditory cortex seed area
 113 at (64, -24, 6), defining the distributed source condition. The resolution of the grid chosen for dipole
 114 simulation was 5mm and “*ft_prepareLeadfield.m*” code of FieldTrip toolbox was used for this pur-
 115 pose. Dipole moment orientations were assumed to be along the radial direction with respect to the
 116 BEM surface, to retain simplicity. We computed the scalp potentials for EEG at realistic sensor loca-
 117 tions by applying a forward model (Mosher *et al.*, 1999; Baillet *et al.*, 2001) with realistic headshape
 118 using “*ft_dipolesimulation.m*” of the FieldTrip toolbox.

$$v_r(t) = \mathbf{L}^T(r, \mathbf{r}_q) \cdot q(t) \quad (2)$$

119 where, v is the electric potential at sensor location r , r_q represents all source locations, \mathbf{L} represents
 120 the “lead field kernel”, $(.)^T$ represents transpose and $q(t)$ is the dipole moment. Synthetic EEG
 121 data were generated by varying signal to noise ratio (SNR) at the source space. Physiological SNR
 122 was estimated using a statistical measure, $10 \log_{10}[\frac{s}{\sigma_b}]$, where s is peak-to-peak amplitude of EEG
 123 data during rhythmic auditory stimulation (see Experimental Methods below) and σ_b is the standard
 124 deviation of the baseline data. We chose a wide range of SNRs (19 22 25 28 31 dB) to simulate mixture
 125 of Gaussian pulses mimicking transient reponse, both above and below the estimated physiological SNR
 126 level (25 dB), to allow us to evaluate the sensitivity of each method. Further, we introduced time
 127 lags between the signals generated from the left and right hemispheres for two and distributed dipole
 128 models. Time delays of: 0, 15, 30, 45 msec were added to the Gaussian pulse generated from the
 129 right hemisphere. Fig 1 shows simulated EEG activity on scalp surface with bilateral auditory cortical
 130 sources. Following Goldenholz *et al.* (2009), SNR was computed in decibel(dB) using the following
 131 equation.

$$SNR_{dB} = 10 \log_{10} \left[\frac{1}{U} \sum_{u=1}^U \frac{v_u^2}{\eta_u^2} \right] \quad (3)$$

132 where U is total sensor count, v is the signal on sensor $u \in (1, 2, \dots, U)$ provided by the forward
 133 model for a source with unit amplitude. The sensor space variance $\eta_u^2 = \sigma^2(\mathbf{L}\mathbf{L}^T)_u$. Therefore, for each
 134 time lag scenario, we simulated the Gaussian signal of 5 SNR values. Additionally, we also simulated
 135 sinusoidal signals mimicking oscillatory activity with different values of power spectra at 40 Hz. The
 136 power values were chosen with respect to the power spectrum computed for the empirical binaural
 137 condition data, such that the power of simulated sinusoidal at 40 Hz was 50%, 75%, 100%, 125%,
 138 150% of the power at 40 Hz of the binaural condition, illustrated in Fig 1. Further, phase lags were
 139 introduced between the signals generated in left and right hemisphere: $0, \pi/2, \pi$ and $3\pi/2$. Therefore,
 140 all the power ratio scenarios were computed for each phase lag condition.

141 2.2 Source localization methods

142 The basic goal of any source localization technique is to compute the dipolar source locations and
 143 strengths inside the brain from measurements on the scalp (inverse of equation 2). In other words the
 144 objective is to estimate the spatial filter \mathbf{W}_S from the relation

$$q(t) = \mathbf{W}_S \cdot \mathbf{V}(t) \quad (4)$$

145 where, $q(t)$ is the dipole moment at time t , \mathbf{W}_S is the spatial filter matrix, and \mathbf{V} is vector repre-
 146 sentation of all sensor time series. Obviously, the system of equations represented by equation 4 is
 147 ill-posed as number of sensors (dimension of vector \mathbf{V}) are finite, but number of dipoles are unknown.
 148 So, different source localization methods attempt to estimate the \mathbf{W}_S using diverse constraints posed
 149 by anatomy of the brain and functional relationships among brain areas during ongoing task.

150 2.2.1 LCMV

151 Linearly constrained minimum variance (LCMV) belongs to the class of “beamformer” methods that
 152 enhances a desired signal while suppressing noise and interference at the output array of sensors
 153 (Barnes and Hillebrand, 2003). LCMV is built upon an adaptive spatial filter whose weights are
 154 calculated using covariance matrix of EEG/MEG time series data. A spatial filter computes the
 155 variance of the total source power which is allowed to vary but the output of the filtered lead field is
 156 kept constant. As a result the beamformer output is maximized for the target source but other source

157 contributions are suppressed. LCMV attempts to minimize the beamformer output power

$$\mathbf{P} = \mathbf{W}_S^T \mathbf{C} \mathbf{W}_S \quad (5)$$

158 where \mathbf{C} is the data covariance matrix. The entries to spatial filter matrix can be expressed as

$$\mathbf{W}_S = \frac{\mathbf{L}^T \mathbf{C}^{-1}}{\mathbf{L}^T \mathbf{C}^{-1} \mathbf{L}} \quad (6)$$

159 where L is lead field matrix, and following constraint is maintained $\mathbf{W}_S \cdot \mathbf{L}^T = 1$.

160 2.2.2 DICS

161 Dynamic imaging of cortical sources (DICS) beamformer (Gross *et al.*, 2001) works with same con-
162 straint assumption of LCMV but extends the computation of spatial filter to the frequency domain.
163 Here, sensor level cross spectral density (CSD) matrix replaces the covariance matrix and the spatial
164 filter is applied to sensor level CSD to reconstruct the source level CSD of all combination of pairwise
165 voxels. Hence, DICS directly estimates the interaction between sources at respective frequencies. The
166 weight function can be written as

$$\mathbf{W}_S(f) = \frac{\mathbf{L}^T \mathbf{C}^{-1}(f)}{\mathbf{L}^T \mathbf{C}^{-1}(f) \mathbf{L}} \quad (7)$$

167 2.2.3 eLORETA

168 Exact low resolution electrical tomography (eLORETA) (Pascual-Marqui, 2007) combines the lead-
169 field normalization with the 3D Laplacian operator under the constraint of smoothly distributed
170 sources. Compared, to DICS and LCMV where the constraint equation $\mathbf{W}_S \cdot \mathbf{L}^T = 1$ is used, eLORETA
171 seeks to minimize the product $\mathbf{H} = \mathbf{W}_S \cdot \mathbf{L}^T$.

$$\mathbf{W}_S = [\mathbf{L}^T (\mathbf{L} \mathbf{C}^{-1} \mathbf{L}^T + a \mathbf{H})^+ \mathbf{L}]^{1/2} \quad (8)$$

172 where ‘ a ’ is regularization parameter, $+$ is the Moore-Penrose pseudo-inverse which is equal to the
173 common inverse if the matrix is non-singular. \mathbf{H} is also called the centering matrix or the surface
174 Laplacian. Low resolution imaging results in weak performance for recovering of multiple sources
175 when the point-spread functions of sources overlap. Other methods have also tried to combine surface

176 Laplacian with LCMV (Murzin *et al.*, 2013), to estimate source-level connectivity.

177 2.3 MNE

178 Minimum norm estimates (MNE) has been a popular choice to localize evoked activity and tracking
 179 the distribution of the activations over a period of time. MNE is a distributed inverse solution that
 180 discretizes the source space into locations on the cortical surface or in the brain volume using a
 181 large number of equivalent current dipoles. It estimates the amplitude of all modeled source locations
 182 simultaneously and recovers a source distribution with minimum overall energy that produces observed
 183 sensor data consistent with the measurement (Hämäläinen and Ilmoniemi, 1994; Ou *et al.*, 2009). The
 184 current density q can be calculated as

$$\mathbf{q} = [\mathbf{C}\mathbf{L}^T(\mathbf{L}\mathbf{C}\mathbf{C}^T + \lambda\mathbf{C})^{-1}] \quad (9)$$

185 2.4 Measurements used for face validity of inverse algorithms:

186 Using simulated data to test a method provides mechanism for ground truth validation. The exact
 187 location of a putative dipolar source is elusive in nature for real data, however, one can certainly
 188 set-up simulations when performance of a particular method needs evaluation. We employed three
 189 complementary measures to provide face-validity of the eLORETA in comparison with LCMV and
 190 DICS.

191 1. Localization error estimation:

192 Inverse methods estimate a cluster of point dipolar sources. To measure how much error is
 193 involved in source localization, we first computed the z-scores for all voxels. Further, we thresh-
 194 olded the z-scores at 99.99th percentile and identified the cluster closest to the dipole location.
 195 Then we measured the Euclidean distance between the voxel with the maximum z-score of the
 196 nearest cluster source points and the actual source/dipole coordinates, to give us the ‘Localiza-
 197 tion Error’. This was done for each hemisphere, separately. Consequently, the net localization
 198 errors are computed by summing up across two hemispheres and compared for eLORETA, MNE,
 199 LCMV and DICS.

200 2. Degree of Focal localization: The size of a cluster in terms of sum of distances of all points from

201 the voxel with the maximum z-score, gives a measure of focal localization of sources. Post finding
202 the z-scores of all voxels, we thresholded the scores at 99.99th percentile and identified the cluster
203 of source points closest to the dipolar location. Further, we computed the total sum of distances
204 of each voxel in the nearest cluster, from the voxel in the cluster with the maximum zscore,
205 as a measure of the spatial distribution of the estimated source. This gave us a quantitative
206 approach to evaluate the degree of focal source localization. For practical reasons, cluster width
207 computation was done for each hemisphere separately Murzin *et al.* (2013).

208 3. Performance evaluation at various depths: The localization of deep sources has been the main
209 factor limiting detection of true sources from M/EEG data. This is important since deep cortical
210 areas constitute 30% of the cortical sources (Hillebrand and Barnes, 2002). We studied the effects
211 of depth by positioning the dipoles at different distances from the auditory cortical locations
212 mentioned earlier. The depth was varied along the x-axis, from 0 to 20 mm in steps of 1 mm,
213 towards the center of the brain, in both hemispheres. Further, we computed the localization
214 error and the focal width of the significant voxels obtained by localizing the dipoles placed at
215 each depth. This was executed using the distributed dipolar method only. All simulated signals
216 were added to the empirical baseline to retain the physiological SNR for the Gaussian pulses and
217 the physiological power spectrum for the sinusoidal. The signals simulated were phase-locked
218 (sinusoidal) and no time lags were added (Gaussian)

219 4. Performance evaluation with various correlation: Correlation in the data covariance is an im-
220 portant variable which can influence localizing capabilities of beamformers (Belardinelli *et al.*,
221 2012). Therefore, we simulated multiple signals using the distributed dipolar model, consequently
222 adding with the empirical baseline, such that there are various phase lags between the signal
223 simulated in the left hemisphere and the right hemisphere. 4 phase lags chosen for frequency do-
224 main analysis were $0, \pi/2, \pi, 3\pi/2$. The power ratios were matched as per the acquired empirical
225 power ratios. 4 time lags chosen for time domain analysis were: 0, 15 30 45 msec.

226 5. False positive percentage: We compared the “sensitivity” and “specificity” of eLORETA, LCMV
227 and DICS, using ROC analysis (Metz, 1978). Here, we calculated the probability of incorrectly
228 detecting an activation, also called ‘false positive (FP)’. Ideal detection should suppress FP. After
229 thresholding the z-scores, we identified the number of significant clusters in each hemisphere,

230 visually. Further we ran k-means clustering over significant voxel locations in each hemisphere
231 and identified the nearest cluster to the *true* dipole location. Defining the nearest significant
232 cluster/s from the dipolar location/s as the true positive/s, we further defined the false positive
233 percentage by computing the ratio of number of significant voxels not present in the true positive
234 (or nearest cluster) and the total number of significant voxels. We also compare the performance
235 of all methods under parametric variation of signal to noise ratio at the source level and different
236 kinds of source configurations, e. g., single point dipole, 2-point dipoles and distributed dipoles.

237 6. Hit rate: To evaluate the accuracy of localizing algorithms, we computed the hit rate or true
238 positives for each method. Post thresholding the z-scores and obtaining the significant clusters
239 (using k-means), we identified the number of significant source points in the nearest cluster
240 within a distance of 15 mm from the simulated dipole location. These source points were defined
241 as hits. The hit rate corresponds to the ratio of number of hits and total number of significant
242 source points in the nearest cluster. Hit rates were calculated across all SNR's and power ratios,
243 including lags and different phase differences respectively for single point, 2-point and distributed
244 dipoles.

245 **2.5 Code Accessibility**

246 All codes used for simulation of data and source localization algorithms is available at the following
247 GitHub repository <https://github.com/arpan-toolboxes/QuantitativeSourceImaging>. Reader
248 is encouraged to contact the authors in case of implementation issues.

249 **2.6 Empirical EEG recordings**

250 **Participants**

251 10 healthy volunteers (8 males, 2 females) aged between 22–39 years (mean age 28 years) participated
252 in the study after giving informed consent, following the guidelines approved by Institutional Human
253 Ethics Board at National Brain Research Centre. All participants were self-declared normal individuals
254 with no history of hearing impairments, had either correct or corrected-to-normal vision and no history
255 of neurological disorders.

256 **Stimuli**

257 Volunteers had to remain stationary in a seated position within a sound-proof room and hear auditory
258 stimuli through 10 Ohm insert earphones with disposable foam ear-tips, binaurally for 200 seconds
259 while fixating at a visual cross. Additionally they had a baseline block where they fixated at the visual
260 cross for 200 seconds without any sounds being played. Sounds were pure tones of 1000 Hz frequency
261 and 25 millisecond time duration, with 5% rise and fall times and were repeated with a frequency of
262 40 Hz during an 'On' block of 1 second duration interspersed between 2 'Off' blocks where no auditory
263 stimuli were presented. Stimuli were made using in STIM2 stimulus presentation system with audio
264 box P/N 1105 at 85 dB.

265 **Data Collection and Pre-processing**

266 EEG data was acquired in an acoustically shielded room with 64 channels NeuroScan (SynAmps2)
267 system with 1 KHz sampling rate. Brain Products abrasive electrolyte gel (EASYCAP) was used to
268 make contact with scalp surface and the impedance was maintained at values less than $5k\Omega$ for all
269 volunteers. Baseline EEG data was recorded for 200 seconds with eyes open, no tone, and a fixation
270 cross on a monitor in front of the participants. Baseline and binaural stimuli were presented while
271 participants were asked to maintain fixation on the cross all along to reduce eye movements.

272 Recorded raw data were re-referenced with average reference and were detrended to remove linear
273 trends from the signal. Epochs of 5 second duration were constructed by concatenating 'ON' blocks of
274 1 second each, after removal of an initial 50 seconds of the 200 seconds long session. This was done to
275 capture auditory steady state responses (ASSR). Data were band pass filtered with cutoff frequencies
276 5-48 Hz, to concentrate on sources underlying ASSR.

277 For an evoked waveform analysis, after average re-referencing, epochs of 1 second duration of
278 'ON' blocks were extracted from the raw data during stimulus condition, then filtered with cut-off
279 frequencies 0.5-48Hz, detrended and averaged across trials to generate the evoked potential. Thresholds
280 of $-100\mu V$ and $100\mu V$ were used to reject blink-corrupted trials, meaning if at any point within the
281 epoch, the voltage exceeded the threshold values, the entire trial was deleted from the subsequent
282 analysis.

283 Sensor locations were taken from the template given in the fieldtrip toolbox. Colin 27 struc-

284 tural T1 was used for co-registration with the sensor locations for accurate source localization. A
285 forward model was computed using Boundary Element Method (BEM) from the respective T1-
286 image. For localization using the algorithms, we considered 0 % regularization for all methods.
287 The ratio of source power between stimulus and baseline condition was calculated in each voxel, us-
288 ing $(Power(Stimulus) - Power(Baseline)) / Power(Baseline)$ for the current density measures and
289 $(Power(Stimulus) - Power(Baseline))$ for the beamformers. After computing the source intensities
290 in each volunteer, the individual grids were interpolated to the T1 image. The averaged voxel intensi-
291 ties across all participants were evaluated using non-parametric statistics and z-scores were computed
292 for each hemisphere. The top 0.05% voxels were identified as sources.

293 3 Results

294 3.1 Simulated EEG data

295 Simulated EEG data was computed by placing electric dipolar sources at auditory cortical locations,
296 according to single dipole, two-point dipoles and distributed dipole configurations, using equation 1
297 and projecting the source activity at realistic sensor locations of a Neuroscan (Compumedics Inc,
298 USA) EEG cap using a realistic head model (equation 2, Baillet *et al.*, 2001). We considered two
299 types of temporal profiles for source activity, a sinusoidal signal mimicking the band-specific frequency
300 response observed in typical EEG signal such as auditory steady state response (ASSR) and a mixture
301 of Gaussian pulses representing the time-locked event related potentials (ERP). Baseline data was
302 acquired empirically on which both the aforementioned signals were added. Two prototype examples
303 of simulated scalp activity during task and baseline are illustrated in Fig 1. To observe the effects of
304 correlation in the cross-spectral density matrix on source localization, phase lags were introduced to
305 the simulated sinusoidal signals generated from each hemisphere (2 point and distributed dipoles),
306 as well as, time delay was added to the gaussian pulses to the signal from the right hemisphere in 2
307 point and distributed models.

308 We applied eLORETA and DICS to perform frequency-locked source analysis on the sinusoidal
309 data. Keeping the empirical baseline intact, we scaled the sinusoidal signal such that, we obtained
310 different ratios of power of the sinusoidal at 40Hz, comparable to the values we found in our empirical
311 data. Fig 2a, illustrates combined results from eLORETA and DICS algorithms on a brain surface

312 rendered by the MNI brain, at power ratio of 1 (realistic SNR), for the distributed dipole model.

313 The algorithms were employed for localizing the sources of the peak negative response in mixture
314 of Gaussians signal, by selecting a time segment constituting of points ± 25 ms around the peak (Fig
315 1b). For plotting activations, the source locations in the 3-D voxel space was projected to a surface
316 plot using customized MATLAB codes.

317 The localization error was computed by first defining each voxel as point in a cluster and thereby
318 determining the distance of the voxel with the maximum z-score from the true dipole source in each
319 hemisphere. For distributed dipolar sources, the centre of the spherically distributed source was
320 considered as the true dipole location. The average of sum of distances from all such points to the
321 voxel with the maximum z-score, normalized by the total number of points was used to quantify the
322 focal localization of sources, in each hemisphere. All voxels were then transformed to their nearest
323 projections on the cortical surface and identified as possible source locations in Fig 2. The quantitative
324 evaluation of the performances of the inverse methods are addressed as follows.

325 **Accuracy:**

326 Frequency analyses using eLORETA and DICS yielded similar localization errors with respect to dif-
327 ferent power ratios, in 1 dipole condition giving 0 false positives (Fig 3). However, eLORETA provided
328 much lower localization error than DICS for 2 point and distributed dipole conditions. This was ob-
329 served at lags: $0, \pi/2$ and $3\pi/2$, where DICS performed comparatively poorly. Interestingly, DICS
330 performed better than eLORETA at phase lag of π in terms of accuracy, at which eLORETA's accu-
331 racy deteriorated. Overall, the most significant observation was linked to the consistent performance
332 of the algorithms regardless of the power spectra at 40 Hz.

333 In time domain analysis, eLORETA performed better in all dipole configurations in contrast to
334 MNE and LCMV (Fig 4). eLORETA consistently provided localization error of around 1cm or less for
335 all time lags. LCMV's accuracy with respect to SNR's and time lags was not consistent as no trend
336 could be observed. In contrast, MNE was observed to be better than LCMV at almost all scenarios
337 with consistent errors across all SNRs. Therefore, it can be pointed that SNR and time lags affect the
338 performance of the beamformers and minimal effects can be found in the current density measures, in
339 terms of accuracy.

340 **Localization Spread:**

341 eLORETA performance is observed to be comparable (similar focal localization) to DICS across all
342 dipole conditions, as well as, power ratios (Fig 3). Apart from slightly higher values of focal localization
343 for DICS at $\pi/2$ lag, both algorithms are efficiently focal.

344 The focal localization of eLORETA on timelocked signal was observed to reduce for single and
345 2 dipole condition, across different SNRs, however not varying across time lags (Fig 4). MNE and
346 LCMV performance was comparable and also didnot vary across time lags. However, the focal width
347 of eLORETA deteriorated in the distributed dipole condition and varied heavily across time lags, in
348 contrast to unperturbed performance of LCMV and MNE. Additionally, the focal width of eLORETA
349 increased with increasing SNR. However, it was noted that there was minimal effect of SNR on the
350 focal width of the other algorithms.

351 **Depth:**

352 To quantitatively measure the localizing capabilities of eLORETA, DICS, MNE and LCMV, source
353 localization was executed for distributed dipoles at different depths. The localization error and the
354 focal width were computed for the significant voxels, illustrated in Fig5. The depth of dipolar locations
355 was varied along the x-axis according to the MNI template, $1mm$ apart for each localization iteration.
356 The deepest positions were selected as $[-40, -28, 6]$ in the left hemisphere and $[40, -24, 6]$ in the right
357 hemisphere. The locations closest to the surface were chosen as $[-60, -28, 6]$ in the left hemisphere and
358 $[60, 28, 8]$ in the right hemisphere.

359 The localization error for DICS declined and performed favourably as the depth of the dipoles
360 decreases. A difference of 10 mm was observed between the deepest and the most superficial source
361 for DICS. However, eLORETA gave consistent low localization errors across all depths. It is observed
362 to be more focal than DICS across all depths, except for comparable focal width for superficial sources.

363 For the time-locked condition, the current density measures performed better than the beamformer,
364 for localizing the Gaussian signal at all depths (performance of eLORETA>MNE>LCMV). Although
365 LCMV was found to be more focal at certain depths, eLORETA and MNE were found to be focal
366 across varying depths. eLORETA proved to be slightly more focal than MNE at deeper depths, in
367 contrast to MNE being more focal the eLORETA at smaller depths. Therefore, eLORETA can be

368 credited to have a higher degree of focal localization in comparison to MNE, LCMV and DICS, for
369 localizing sinusoidal, as well as, Gaussian pulse, especially at deeper depths.

370 **False positive percentage:**

371 To evaluate specificity, we computed the false positives after applying DICS, LCMV and eLORETA
372 in different SNR scenarios, for all phase/time lags across different dipole conditions. All source points
373 except the cluster of points nearest to the dipole location were considered as false positives (see section
374 2.4 for details).

375 With 0 false positives for 1 dipole condition, the false positives of DICS increased with increasing
376 number of dipoles (Fig 3). With the percentage ranging from 30-70 percent, eLORETA provided a
377 very high rate of true positives across all SNR's and phase lags. Unsurprisingly, eLORETA gave a
378 very low false positive fraction on localizing the Gaussian, similar to localizing the sinusoidal (Fig 4).
379 MNE and LCMV gave high and comparable but consistent false positives fraction across all time lags
380 in single and 2-dipole condition. However, in the distributed dipole case, the false positives of MNE
381 and LCMV increased with varying time lags.

382 Table 1 classifies the performance of all the methods based on accuracy, localization and sensitivity
383 across all dipole conditions for localizing 40 Hz sinusoidal signal (frequency analysis) and Gaussian
384 pulse response (time-lock) respectively.

385 **Hit rate:**

386 eLORETA and DICS proved to be reliable in localizing single dipole, by yielding 100 percent hit rates
387 at SNRs of biological level and higher. However, DICS indicated varied results with respect to the
388 different power ratios at 40 Hz between the simulated and empirical data. In both, distributed and two
389 point dipolar model as the hit rates plummeted at phase difference of π . In contrast, eLORETA had
390 high hit rates irrespective of phase differences and further increased with higher number of dipoles.
391 For algorithms localizing the temporal features of the signal, the beamformer LCMV's performance
392 was influenced by SNR i.e. hit rates increased with increasing SNR's across all models. However, this
393 was not true for the current density measures, since they were minimally influenced by SNR. Despite
394 almost perfect localization of single dipole by current density measures, eLORETA yielded higher hit
395 rates compared to MNE in two point and distributed dipole models. Similar to DICS, the hit rates

396 corresponding to LCMV varied with respect to different temporal lags. To summarise, eLORETA's
397 hit rates were superior amongst beamformers and current density measures.

398 **3.2 Empirical EEG data**

399 **Source localization underlying 40Hz EEG activity**

400 The Fourier spectrum of each EEG channel time series were computed by multi-taper method with
401 number of tapers = 2, using Fieldtrip function `ft_freqanalysis.m`. Power spectral density of empirical
402 EEG data and the ERP time locked to the onset of a single tone stimulus are shown in Fig 6. In
403 Fig 6a, the topoplot of the difference in power between binaural and baseline conditions at 40 Hz
404 is shown along with the log of power across all trials. There are peaks at alpha band 8-12 Hz in
405 both binaural and baseline conditions the difference between which was not significant (two-sample
406 $t = -0.018, p = 0.95$) whereas the binaural condition had a sharp rise in power at 40 Hz which was
407 significant (two-sample $t = 0.18, p < 0.0001$). The t-tests were performed on logarithm of power
408 spectrums from two conditions within a frequency bands, 8 – 12 Hz for alpha and 39.8 – 40.2 Hz for
409 evoked 40 Hz. Localization results are illustrated in Fig 7 a. The left, top and right views of activation
410 are shown where red regions represent sources from eLORETA analysis while green regions represent
411 activation plots generated by DICS.

412 Acknowledging the absence of ground truth concerning true sources that exist in empirical data,
413 we evaluated the focal width of all the significant clusters post thresholding the z-scores. 1 such cluster
414 was found in each hemisphere around the auditory cortex for eLORETA, providing a mean focal width
415 of $3.958mm$. In contrast, DICS yielded 1 cluster at the auditory cortex in the left hemisphere and
416 7 distributed clusters in the right. The mean focal width across DICS clusters was $2.8324mm$, lesser
417 than that of eLORETA. Understanding that the thresholding can vary focal width and number of
418 clusters, we maintained the same threshold for both the algorithms for a fair comparison. It is to be
419 noted that the mean focal width of 2 clusters of eLORETA can be decreased with higher thresholding.

420 **Source localization of N100 response**

421 In Fig 6b we show the ERP responses to the binaural tone and the ERPs in baseline condition,
422 averaged across all trials and participants (grand average). A negative peak around 100 ms post onset

423 of tone stimulus (N100) was observed in the binaural condition with a latency of around 110 ms. The
424 topoplot represents the spatial map of the difference in relative changes of amplitude between ERPs
425 from the the binaural and baseline conditions across all channels and trials.

426 Next, we computed the underlying source activation during the N100 response using LCMV and
427 eLORETA. In Fig 7b we plot the source activations (top 0.05% voxels similar to 40Hz case) in epochs of
428 duration 50 ms, within which the 25th ms corresponds to the peak of N100. The beamformer localized
429 bilateral auditory cortices, along with other distributed significant clusters. It can noted that LCMV
430 may localize the underlying activity, however, has higher probability of yielding false positives, due to
431 its distributed activations. In contrast, the current density measures localized the left auditory cortex
432 (eLORETA) and left posterior superior temporal sulcus (MNE). Computing only 1 cluster for each
433 hemisphere, eLORETA and MNE yielded a significant cluster in the right frontal regions. The focal
434 width of LCMV (2.1706 mm) was lesser than current density measures (3.1-3.3 mm), similar to the
435 case in the frequency domain analysis.

436 4 Discussion

437 Identifying the sources underlying key events of information processing such as ERP peaks or oscilla-
438 tory brain activity such as spontaneous gamma oscillations are the objectives of many research studies.
439 However, different inverse methods provide different solutions leading to no agreement of which algo-
440 rithm is the ‘best method’, as we illustrated in this manuscript with simulated and empirical EEG
441 data. Even though the selection of the best method can be guided by the nature of the hypothesis in
442 a putative experimental design, a systematic comparative account of the efficacies of few prominent
443 methods is currently missing in the literature. To address this issue we compared methods, eLORETA
444 (Pascual-Marqui, 2007), LCMV (Van Veen *et al.*, 1997), MNE (Hämäläinen and Ilmoniemi, 1994) and
445 DICS (Gross *et al.*, 2001) using the metrics that evaluates accuracy, sensitivity and specificity across
446 three dipolar models (single, two-point and distributed) for the simulated sinusoidal signal (mimick-
447 ing the steady state 40 Hz) and a mixture of Gaussian pulses (representing the time locked ERP).
448 Furthermore, we chose an empirically observed baseline which is a key ingredient for every inverse
449 method. The models were simplistic, however, since we knew the exact location of dipole/s, ground
450 truth validation was possible. All methods are able to retrieve the location of the true dipolar sources

451 for a physiologically relevant SNR and frequency power ratio (blue areas in Fig 2). Nonetheless,
452 the study was conducted across different SNRs and frequency power spectra to test each method's
453 sensitivity and specificity to noise. Furthermore, performance of all methods were evaluated with
454 respect to dipolar depth, phase lags among sources, accuracy and localization spread over space. Also,
455 we conducted source localization by collecting empirical EEG data exhibiting 40 Hz ASSR (Fig 7).
456 DICS and eLORETA were used to compute the sources underlying the 40 Hz activity and LCMV
457 and eLORETA were used to compute the sources underlying the N100 response (Fig 7). Thus, we
458 could outlay the hallmarks of each method in a organized framework. The key finding of our study
459 is that even though high hit rates and focal localization are achieved with both current density and
460 beamformer approaches, the false positives and focal width of sources needs to be carefully considered
461 while choosing a specific method and this is where eLORETA scores above most of the other methods.

462 A general consensus emerges from comparing the algorithms that there is no clear winner (Table
463 1) if accuracy as well as sensitivity and specificity are all taken together as guiding parameters. DICS
464 gives better accuracy than eLORETA in single and two-point dipole conditions even at low SNRs,
465 however, the focal width of eLORETA generated sources are always slightly better most likely due
466 to the minimization of the surface Laplacian component while estimation of the spatial filter. For
467 distributed dipole scenario, focal width of eLORETA results were very similar to DICS, in fact getting
468 better with higher SNR. Interestingly, eLORETA shows significant control on the false positive ratio in
469 the distributed dipole condition, proving to be the method of choice for estimating sources underlying
470 frequency response in a more exploratory setting. This is indeed a very important point to note
471 for increasing number of studies studying resting state functional connectivity (Canuet *et al.*, 2011;
472 Custo *et al.*, 2017). Once a hypothesis is put in place with some prior knowledge about the involvement
473 of prospective brain networks one can go for DICS that can produce more accurate results (Tan *et al.*,
474 2016). Interestingly, DICS results in lowest localization error with maximum phase lag of π , whereas
475 the effect was reverse for eLORETA.

476 For source localization of ERP peaks, eLORETA majorly yielded better accuracy and specificity
477 (in terms of favorable false positives) than LCMV and MNE, even though the focal width of eLORETA
478 sources were considerably larger than LCMV and MNE. The pitfalls and advantages of each method
479 are summarized in Table 4. As in case, of frequency domain analysis, we would recommend eLORETA
480 for a exploratory level analysis whereas the LCMV or MNE for more hypothesis driven identification

481 of sources.

482 An alternative solution to increase the probability of isolating an active source is to combine 2 or
483 more methods and take the overlap of sources detected from them as the plausible source configura-
484 tion. We provide a blueprint of these using our empirical and simulated data. Both spectral domain
485 eLORETA and DICS were able to pinpoint the left auditory cortex, the location of one true source (Fig
486 2). The number of false positives obtained with two methods combined are drastically low. This gives
487 us the confidence that ASSR involves strong activity in primary sensory regions of auditory processing
488 e.g., bilateral middle temporal gyrus as reported by earlier studies (McFadden *et al.*, 2014; Tan *et al.*,
489 2016) and as we observe in Fig 7. Although, for current empirical data we did not find overlapping
490 regions from different techniques, validation from 2 or more methods will give a strong confidence in
491 the result of source localization. Proof-of-concept illustration is available for time-lock analysis as well
492 (Fig 7), where we present combined eLORETA, LCMV and MNE to identify the sources underlying
493 N100 peak.

494 In future we think an overlap-approach might result in focal localization with minimum number
495 of false positives. This will particularly benefit the identification of sources whose activity may be
496 relevant for a particular context. For example cross-frequency coupling (CFC) between alpha-gamma
497 rhythms are being postulated to be important for gating of attention (Klimesch, 2012). How to
498 identify a cortical subnetwork whose nodes show CFC out of the whole alpha and gamma networks is
499 an important methodological challenge. We believe a conjunction of methods strategy to identify the
500 potential sources will be crucial from the perspective of reliability as well as accuracy. In summary,
501 our study provides a blue print for employing source-localization techniques to isolate more subtle
502 features of signal processing.

503 References

- 504 Baillet, S., J.C. Mosher and R.M. Leahy (2001). Electromagnetic brain mapping. *Signal Processing*
505 *Magazine, IEEE* **18**(6), 14–30.
- 506 Barnes, G. R. and A. Hillebrand (2003). Statistical flattening of EEG/MEG beamformer images.
507 *Hum Brain Mapp* **18**(1), 1–12.

- 508 Belardinelli, P., E. Ortiz, G. Barnes, U. Noppeney and H. Preissl (2012). Source reconstruction accu-
509 racy of MEG and EEG Bayesian inversion approaches. *PloS One* **7**, e51985.
- 510 Bollimunta, A., Y. Chen, C. E. Schroeder and M. Ding (2008). Neuronal mechanisms of cortical alpha
511 oscillations in awake-behaving macaques. *J Neurosci* **28**(40), 9976–9988.
- 512 Bradley, A., J. Yao, J. Dewald and C-P. Richter (2016). Evaluation of electroencephalography source
513 localization algorithms with multiple cortical sources. *PloS One* **11**, e0147266.
- 514 Bressler, S L. and J A.S. Kelso (2001). Cortical coordination dynamics and cognition. *Trends Cogn*
515 *Sci* **5**(1), 26–36.
- 516 Bressler, S. L., R. Coppola and R. Nakamura (1993). Episodic multiregional cortical coherence at
517 multiple frequencies during visual task performance. *Nature* **366**(6451), 153–156.
- 518 Brovelli, A., M. Ding, A. Ledberg, Y. Chen, R. Nakamura and S. L. Bressler (2004). Beta oscillations
519 in a large-scale sensorimotor cortical network: directional influences revealed by Granger causality.
520 *Proc Natl Acad Sci U S A* **101**(26), 9849–9854.
- 521 Buzsáki, G. and A. Draguhn (2004). Neuronal oscillations in cortical networks. *Science*
522 **304**(5679), 1926–1929.
- 523 Canuet, L., R. Ishii, R.D. Pascual-Marqui, M. Iwase, R. Kurimoto, Y. Aoki, S. Ikeda, H. Takahashi,
524 T. Nakahachi and M. Takeda (2011). Resting-state EEG source localization and functional connec-
525 tivity in schizophrenia-like psychosis of epilepsy. *PLOS One*.
- 526 Cheyne, D. and P. Ferrari (2013). MEG studies of motor cortex gamma oscillations: Evidence for a
527 gamma “fingerprint” in the brain?. *Front Hum Neurosci* **7**, 575.
- 528 Cheyne, D., L. Bakhtazad and W. Gaetz (2006). Spatiotemporal mapping of cortical activity ac-
529 companying voluntary movements using an event-related beamforming approach. *Hum Brain Mapp*
530 **27**(3), 213–229.
- 531 Clark, V. P., S. Fan and S. Hillyard (1995). Identification of early visual evoked potential generators
532 by retinotopic and topographic analyses. *Human Brain Mapping* **2**, 170–187.

- 533 Custo, A., D. Van De Ville, W. M. Wells, M.I. Tomescu, D. Brunet and C.M. Michel (2017). Elec-
534 troencephalographic resting-state networks: Source localization of microstates. *Brain Con-*
535 *nectivity*.
- 536 Edelman, G. and V. Mountcastle (1978). An organizing principle for cerebral function: The unit model
537 and the distributed system. In: *The Mindful Brain*. MIT Press.
- 538 Goldenholz, D. M., S. P Ahlfors, M. S. Hämäläinen, D. Sharon, M. Ishitobi, L. M. Vaina and S. M.
539 Stufflebeam (2009). Mapping the signal-to-noise-ratios of cortical sources in magnetoencephalogra-
540 phy and electroencephalography. *Human brain mapping* **30**(4), 1077–1086.
- 541 Gross, J., J. Kujala, M. Hämäläinen, L. Timmermann, A. Schnitzler and R. Salmelin (2001). Dynamic
542 imaging of coherent sources: studying neural interactions in the human brain. *Proceedings of the*
543 *National Academy of Sciences* **98**(2), 694–699.
- 544 Hämäläinen, M. S. and J. Sarvas (1989). Realistic conductivity geometry model of the human head for
545 interpretation of neuromagnetic data. *IEEE Transactions on Biomedical Engineering* **36**(2), 165–
546 171.
- 547 Hämäläinen, M S and R J Ilmoniemi (1994). Interpreting magnetic fields of the brain: minimum norm
548 estimates. *Medical & biological engineering & computing* **32**, 35–42.
- 549 Hedrich, T, G Pellegrino, E Kobayashi, J M Lina and C Grova (2017). Comparison of the spatial
550 resolution of source imaging techniques in high-density EEG and MEG. *NeuroImage* **157**, 531–544.
- 551 Hillebrand, A. and G.R. Barnes (2002). A quantitative assessment of the sensitivity of whole-head
552 MEG to activity in the adult human cortex. *NeuroImage* **16**(3 Part A), 638–650.
- 553 Hillebrand, A. and G.R. Barnes (2003). The use of anatomical constraints with MEG beamformers.
554 *Neuroimage* **20**(4), 2302–2313.
- 555 Ishii, R, K Shinosaki, S Ukai, T Inouye, T Ishihara, T Yoshimine, N Hirabuki, H Asada, T Kihara, S E
556 Robinson and M Takeda (1999). Medial prefrontal cortex generates frontal midline theta rhythm.
557 *Neuroreport* **10**, 675–679.

- 558 Klimesch, W. (2012). Alpha-band oscillations, attention, and controlled access to stored information.
559 *Trends Cogn Sci* **16**(12), 606–617.
- 560 Kutas, M., G. McCarthy and E. Donchin (1977). Augmenting mental chronometry: the p300 as a
561 measure of stimulus evaluation time. *Science* **197**(4305), 792–795.
- 562 Lina, J M, R Chowdhury, E Lemay, E Kobayashi and C Grova (2014). Wavelet-based localization of os-
563 cillatory sources from magnetoencephalography data. *IEEE transactions on bio-medical engineering*
564 **61**, 2350–2364.
- 565 Liu, A.K., A.M. Dale and J.W. Belliveau (2002). Monte carlo simulation studies of eeg and meg
566 localization accuracy. *Human Brain Mapping* **16**(1), 47–62.
- 567 Llinás, R. R., U. Ribary, D. Jeanmonod, E. Kronberg and P. P. Mitra (1999). Thalamocortical dys-
568 rhythmia: A neurological and neuropsychiatric syndrome characterized by magnetoencephalogra-
569 phy. *Proc Natl Acad Sci U S A* **96**(26), 15222–15227.
- 570 McFadden, K.L., S.E. Steinmetz, A.M. Carroll, S.T. Simon, A. Wallace and D.C. Rojas (2014). Test-
571 retest reliability of the 40 Hz EEG auditory steady-state response. *PLOS One* **9**(1), e85748.
- 572 Metz, C.E. (1978). Basic principles of roc analysis. **8**(4), 283–298.
- 573 Mideksa, K G, N Hoogenboom, H Hellriegel, H Krause, A Schnitzler, G Deuschl, J Raethjen, U Heute
574 and M Muthuraman (2015). Comparison of EEG and MEG in source localization of induced hu-
575 man gamma-band oscillations during visual stimulus. *Conference proceedings : Annual Interna-*
576 *tional Conference of the IEEE Engineering in Medicine and Biology Society. IEEE Engineering in*
577 *Medicine and Biology Society. Annual Conference* **2015**, 8119–8122.
- 578 Mosher, J. C., R. M. Leahy and P. S. Lewis (1999). EEG and MEG: forward solutions for inverse
579 methods. *IEEE Trans Biomed Eng* **46**(3), 245–59.
- 580 Müller, N. and N. Weisz (2012). Lateralized auditory cortical alpha band activity and interregional
581 connectivity pattern reflect anticipation of target sounds. *Cerebral Cortex* **22**(7), 1604–1613.
- 582 Murzin, V., A. Fuchs and J. A. Scott Kelso (2011). Anatomically constrained minimum variance
583 beamforming applied to EEG. *Exp Brain Res* **214**(4), 515–528.

- 584 Murzin, V., A. Fuchs and J. A Scott Kelso (2013). Detection of correlated sources in eeg using com-
585 bination of beamforming and surface laplacian methods. *J Neurosci Methods* **218**(1), 96–102.
- 586 Ou, W., M. S. Hämäläinen and P. Golland (2009). A distributed spatio-temporal EEG/MEG inverse
587 solver. *NeuroImage* **44**, 932–946.
- 588 Pantev, C., O. Bertrand, C. Eulitz, C. Verkindt, S. Hampson, G. Schuierer and T. Elbert (1995). Spe-
589 cific tonotopic organizations of different areas of the human auditory cortex revealed by simultaneous
590 magnetic and electric recordings. *Electroencephalogr Clin Neurophysiol* **94**(1), 26–40.
- 591 Pascual-Marqui, R. D. (2007). Discrete, 3D distributed, linear imaging methods of electric neuronal
592 activity. Part 1: exact, zero error localization. *ArXiv e-prints*.
- 593 Picton, T. W., S. A. Hillyard, H. I. Krausz and R. Galambos (1974). Human auditory evoked potentials.
594 I. Evaluation of component. *Electroencephalogr Clin Neurophysiol* **36**(2), 179–190.
- 595 Ramírez, R.R., D. Wipf and S. Baillet (2010). Neuroelectromagnetic source imaging of brain dynamics.
596 pp. 127–155.
- 597 Sato, M., T. Yoshioka, S. Kajihara, K. Toyama, N. Goda, K. Doya and M. Kawato (2004). Hierarchical
598 Bayesian estimation for MEG inverse problem. *NeuroImage* **23**(3), 806 – 826.
- 599 Srinivasan, Ramesh, William R Winter and Paul L Nunez (2006). Source analysis of EEG oscillations
600 using high-resolution EEG and MEG. *Progress in brain research* **159**, 29–42.
- 601 Tan, H.-R. M., J. Gross and P. J. Uhlhaas (2016). Meg sensor and source measures of visually induced
602 gamma-band oscillations are highly reliable. *NeuroImage* **137**, 37–44.
- 603 Van Veen, B.D., W. van Drongelen, M. Yuchtman and A. Suzuki (1997). Localization of brain elec-
604 trical activity via linearly constrained minimum variance spatial filtering. *IEEE Trans Biomed Eng*
605 **44**(9), 867–880.
- 606 Varela, F., J. P. Lachaux, E. Rodriguez and J. Martinerie (2001). The brainweb: phase synchronization
607 and large-scale integration. *Nature Review Neuroscience* **2**, 229–239.

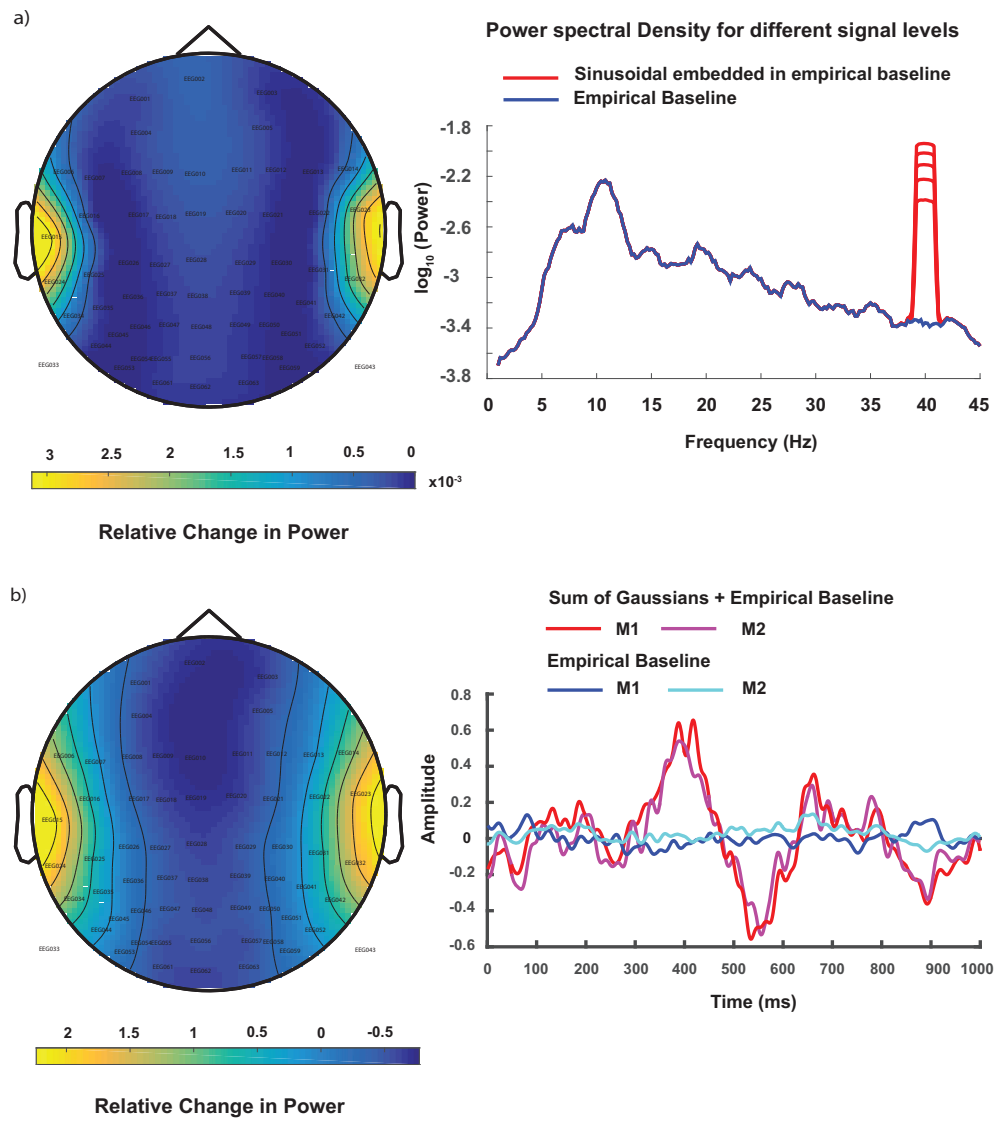


Figure 1: a) Topoplot of the difference in peak of spectral power at 40 Hz obtained from simulated EEG data where dipolar source time series was represented by a sinusoidal signal with frequency 40Hz embedded in empirical resting state EEG and empirical resting state EEG as baseline. Spatially averaged power spectra obtained from averaging the channel-by-channel spectrum from hypothetical scalp sensors are plotted in logarithmic scale. The time series on the scalp were obtained by applying forward modeling techniques on dipolar sources at auditory cortex locations using the boundary element method (BEM) b) Topoplot of the peak of difference signal when a mixture of Gaussian pulses was used to simulate ERP and empirical resting state EEG as baseline in BEM model as described in (a). The time series for dipole dynamics are plotted at hypothetical M1 and M2 sensors located near to the auditory cortices. The positive peak at 400 ms was used for generating the topoplot.

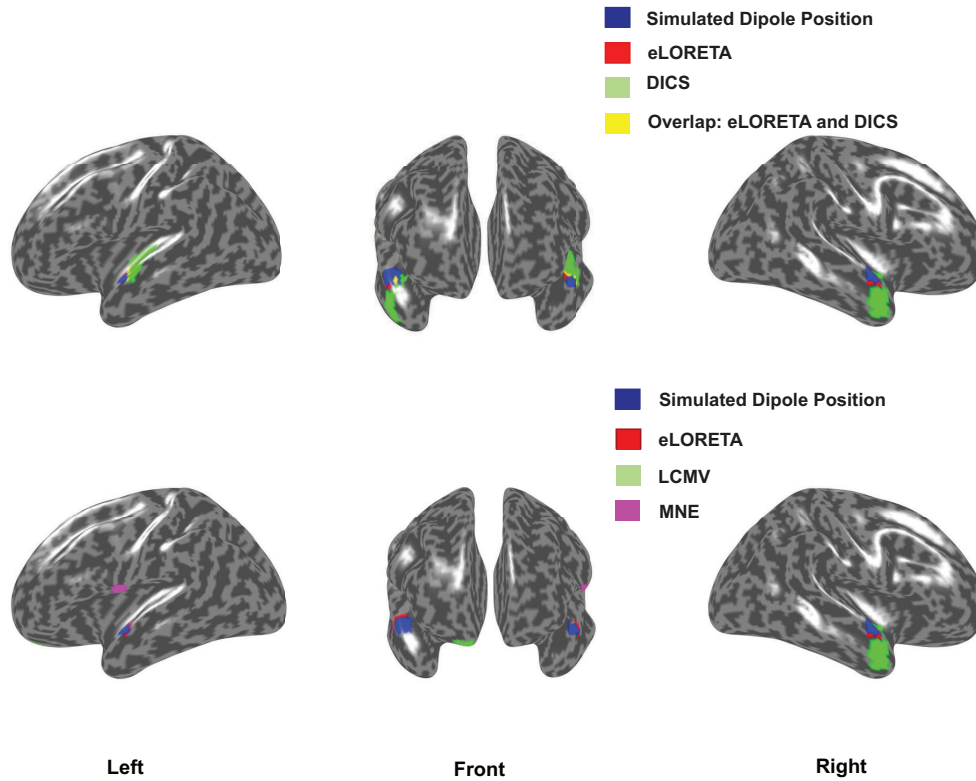


Figure 2: a) eLORETA (red) vs DICS source localization (green) using frequency-lock analyses on distributed dipolar source generated signals. Overlapping regions from both analyses are depicted in yellow and locations used for simulated dipole placements are depicted in blue. eLORETA was applied to the simulated sinusoidal signal embedded in resting state EEG, where the simulated signals generated from each hemisphere had 0 phase lag. For DICS, the simulated signal from the right hemisphere had a phase lag of π with respect to the signal from the left hemisphere. The ratio of power spectrum at 40 Hz between the sinusoidal embedded in EEG and resting state EEG was chosen similar to the ratio found in our empirical results. b) eLORETA (red), LCMV (green) and MNE (purple) generated sources using time-lock analysis. No overlapping regions were found. The results indicate 0 time lag scenario between the Gaussian pulses from each hemisphere. Physiologically realistic SNR 25 dB for simulated dipolar sources was chosen for this illustration.

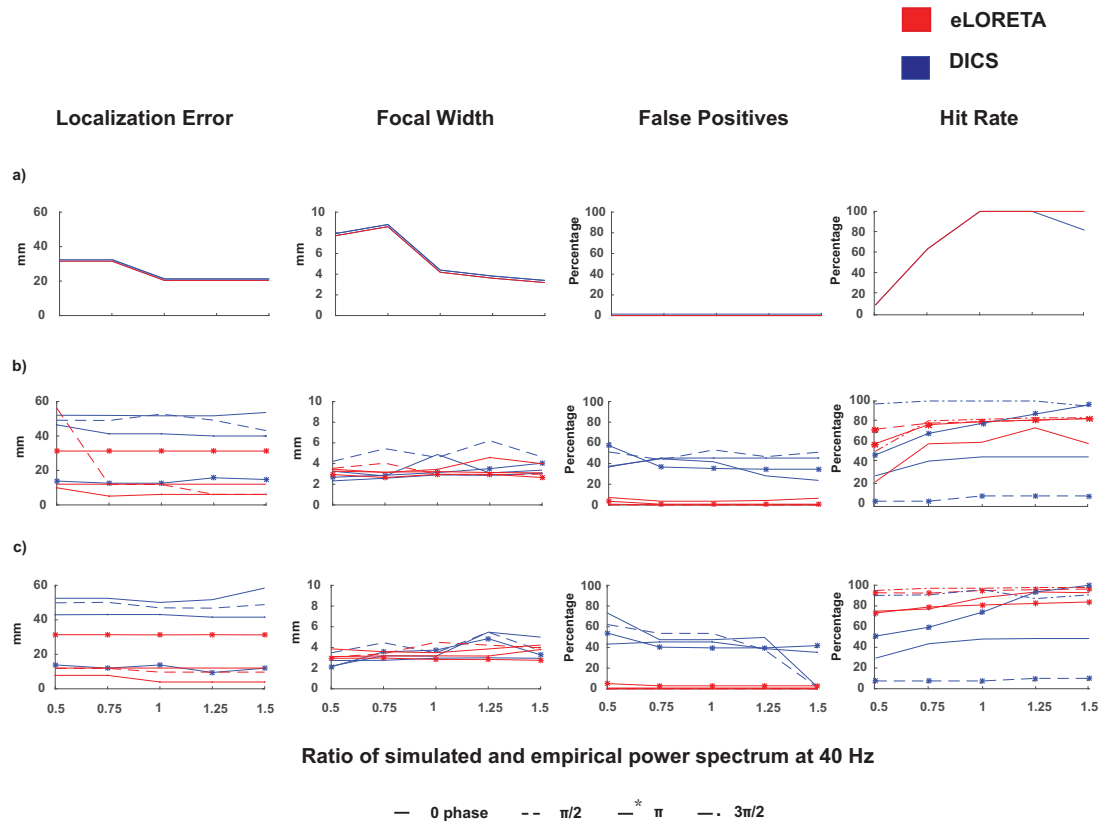


Figure 3: Localization error, Focal width, False positive and Hit rate percentage for (a) Single dipole (b) Two-point dipole and (c) Distributed dipole conditions measured for eLORETA (red) and DICS (blue). Source localization was done for all power ratios (x axis) across different simulated phase lags of $0, \pi/2, \pi$ and $3\pi/2$.

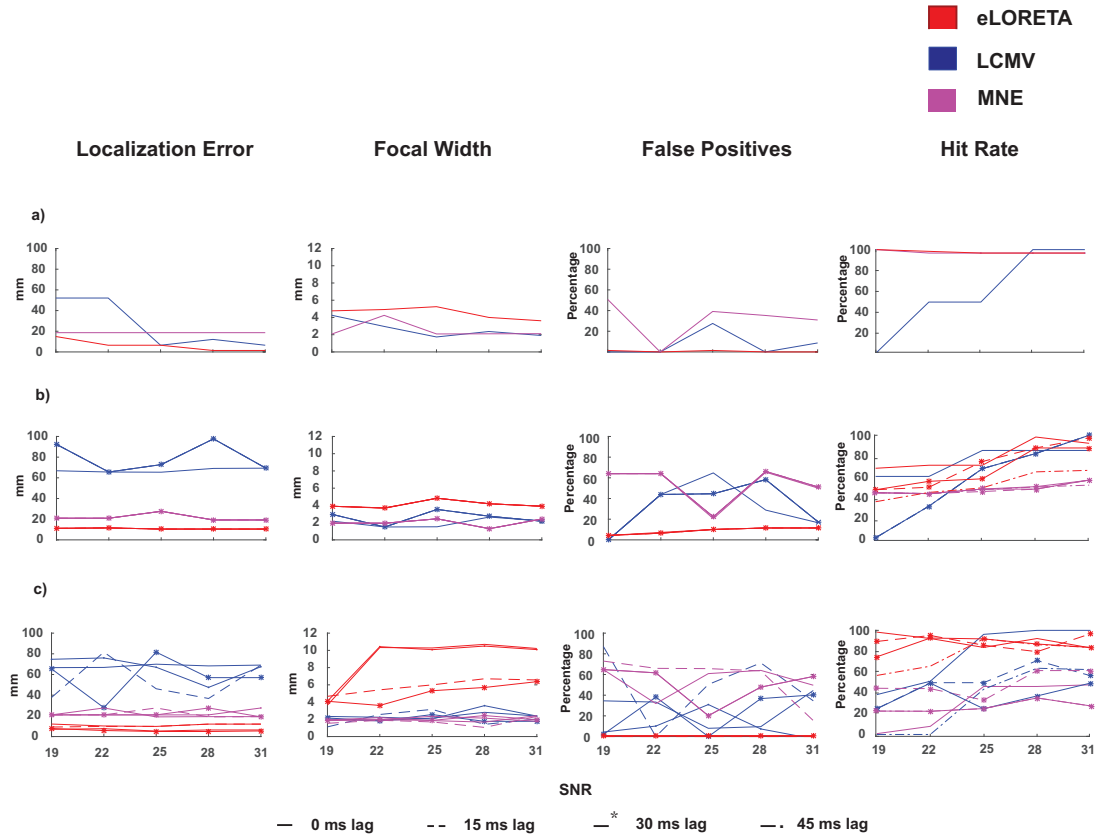


Figure 4: Localization error, Focal width, False positive and Hit rate percentage for (a) Single dipole (b) Two-point dipole and (c) Distributed dipole condition measured for eLORETA (red), LCMV (blue) and MNE (pink). Source localization was done for all SNR's (x axis) across different simulated time lags where 25dB refers to the realistic scenario.

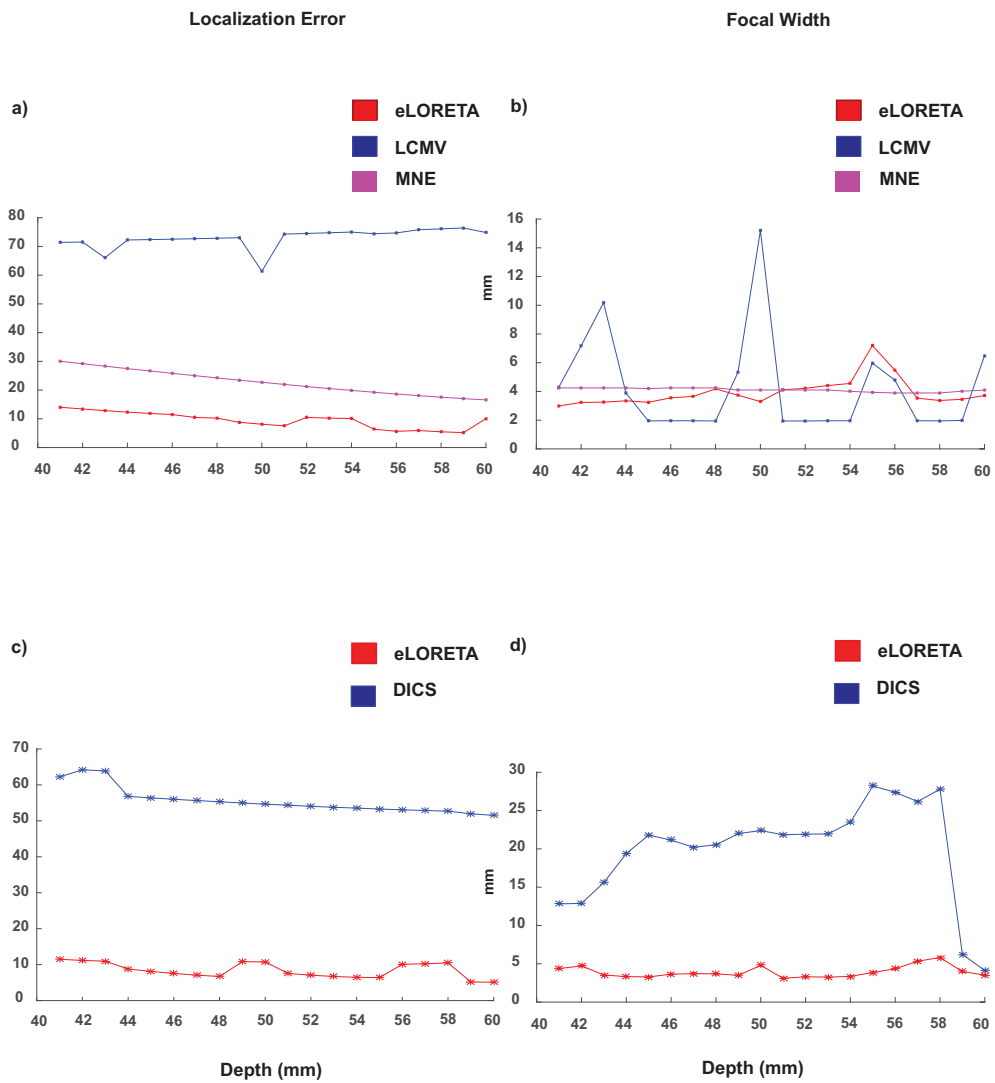


Figure 5: Localization errors and focal widths of all significant voxels computed for simulated distributed dipoles with the centre of the dipole cluster located at different depths from the auditory cortical locations. The depth of the dipoles decrease along the x-axis; the distance from the auditory cortex. (a) and (b) show the localization error and the focal width of the sources generated by the mixture of Gaussian signals respectively. (c) and (d) exhibit the localization error and focal width for frequency domain analysis.

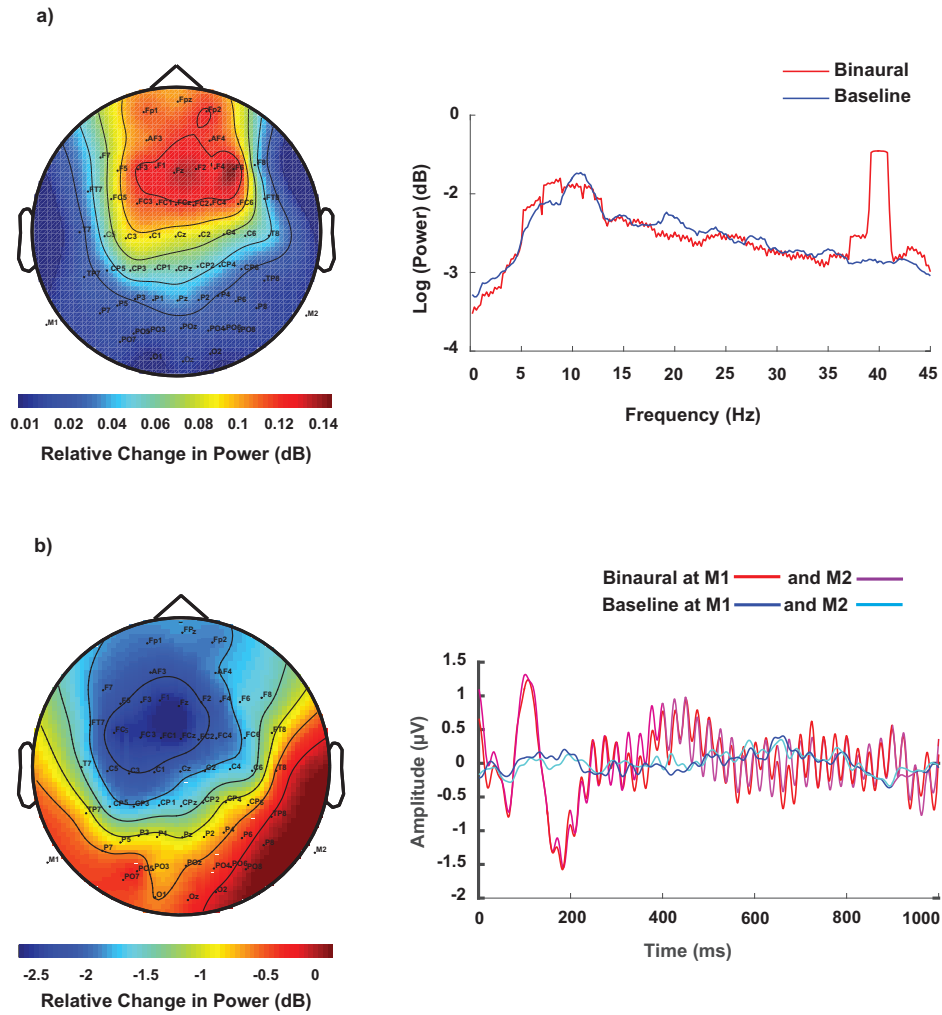


Figure 6: a) Topoplot of spectral power difference at 40 Hz and grand average of spectral power across all sensors, trials and participants in binaural and the baseline conditions. Power spectral density was calculated for 5 sec windows after rejecting an initial 50 sec out of total duration of 200 seconds for which the rhythmic tones were played. b) ERP responses of channels M1 and M2 across trials and participants for binaural and silent baseline conditions and the topoplot for the difference signal at the peak of N100 response (at 110 ms).

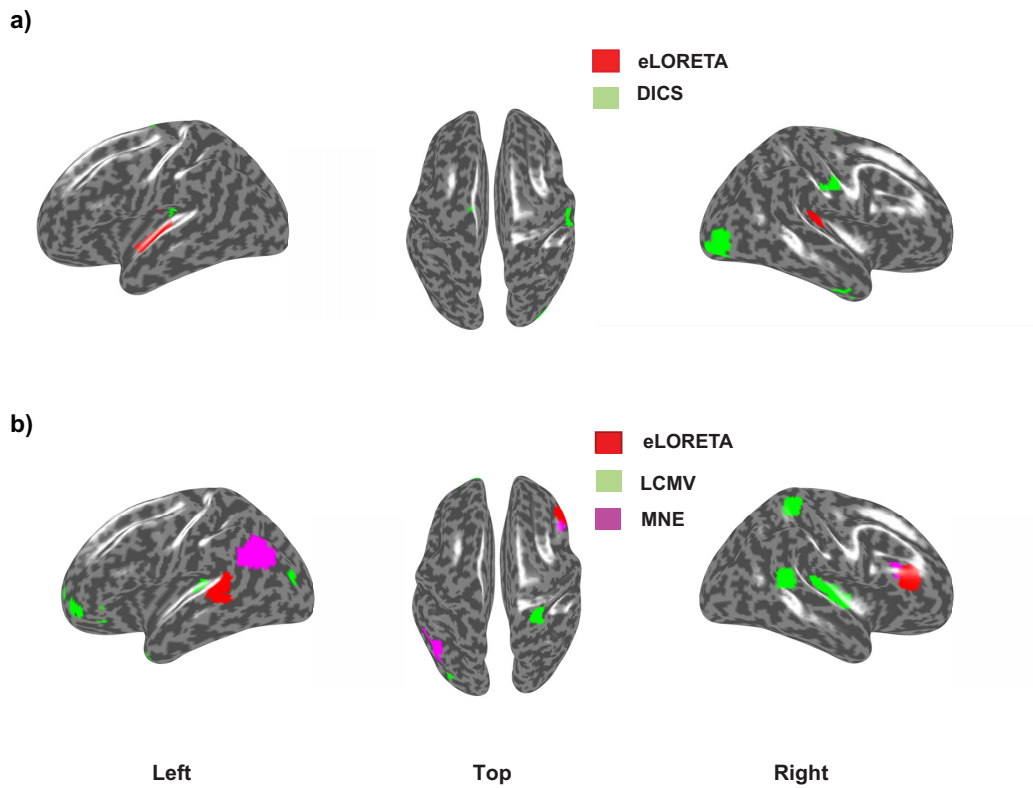


Figure 7: Left, top and right view of significantly active cortical sources underlying for a) 40 Hz auditory steady state response (ASSR) b) N100 component of the event related potential (ERP). The red colored regions show estimated sources from eLORETA while green regions show estimated sources from a) DICS and b) LCMV analysis. The pink regions in b) show MNE source localization results.

a) Frequency Analysis			
Dipole Condition	Localization Error	Focal Width	False Positives
Single Dipole	eLORETA/DICS	eLORETA/DICS	eLORETA/DICS
Two-point Dipoles	eLORETA($0, \pi/2, 3\pi/2$) DICS(π)	/eLORETA	eLORETA
Distributed Dipoles	eLORETA($0, \pi/2, 3\pi/2$) DICS(π)	/eLORETA	eLORETA
b) Time-lock Analysis			
Dipole Condition	Localization Error	Focal Width	False Positives
Single Dipole	eLORETA	MNE/LCMV	eLORETA
Two point Dipoles	eLORETA	MNE/LCMV	eLORETA
Distributed Dipoles	eLORETA	MNE/LCMV	eLORETA

Table 1: Outcome of source localization performance based on different metrics for a) frequency analyses, eLORETA, DICS and b) time domain analyses, eLORETA, LCMV, MNE. If similar performance was achieved, both methods are mentioned with '/'.